High-Fidelity Strain and Temperature Measurements of Li-Ion Batteries Using Polymer Optical Fiber Sensors

Julien Bonefacino, Sasan Ghashghaie, Tianye Zheng, Chun-Pang Lin, Wenwei Zheng, Laura Albero Blanquer, Jiaqiang Huang, Charlotte Gervillié, Hwa-Yaw Tam, J.-M. Tarascon, et al.

OPEN ACCESS

High-Fidelity Strain and Temperature Measurements of Li-Ion Batteries Using Polymer Optical Fiber Sensors

Journal of The Electrochemical Society, 2022 **169** 100508

High-Fidelity Strain and Temperature Measurements of Li-Ion Batteries Using Polymer Optical Fiber Sensors

Julien Bonefacino,[1,2,=,z] Sasan Ghashghaie,[3,=] Tianye Zheng,[1,3] Chun-Pang Lin,[3,4] Wenwei Zheng,[5] Laura Albero Blanquer,[2,6,7] Jiaqiang Huang,[8,9] Charlotte Gervillié,[2,6] Hwa-Yaw Tam,[1] Jean-Marie Tarascon,[2] and Steven T. Boles[3,10,*,z]

[1]*Department of Electrical Engineering, The Hong Kong Polytechnic University, Kowloon, Hong Kong, People's Republic of China*
[2]*Collège de France, Chimie du Solide et de l'Energie—UMR 8260 CNRS, Paris, France*
[3]*Centre for Advances in Reliability and Safety, New Territories, Hong Kong, People's Republic of China*
[4]*Rutgers University, New Jersey, United States of America*
[5]*GP Batteries International Limited, 7/F, 16W, Hong Kong Science Park, Hong Kong*
[6]*Réseau sur le Stockage Electrochimique de l'Energie (RS2E)—FR CNRS 3459, 80039 Amiens Cedex, France*
[7]*Sorbonne Université—UPMC Paris 06, 4 Place Jussieu, 75005 Paris, France*
[8]*The Hong Kong University of Science and Technology (Guangzhou), Sustainable Energy and Environment Thrust, Nansha, Guangzhou, Guangdong, 511400, People's Republic of China*
[9]*HKUST Shenzhen-Hong Kong Collaborative Innovation Research Institute, Futian, Shenzhen, Guangdong, People's Republic of China*
[10]*Department of Energy and Process Engineering, Faculty of Engineering, Norwegian University of Science and Technology (NTNU), Trondheim, Norway*

The convergence of fiber optic sensing with lithium-ion batteries holds great promise for observing key cell parameters in real time, which is essential to every level of decision making, from design and engineering to finance and management. Optical sensors based on fiber Bragg gratings have recently been demonstrated as an ideal tool for measuring these metrics with sufficient temporal and spatial resolution. In this work, we extend the use of fiber Bragg gratings to polymeric optical fibers which have notably greater thermal and strain coefficients than their common silica counterparts. We demonstrate that a polymer optical fiber sensor paired with a silica-based sensor, both affixed to the external package of a lithium battery, can concurrently generate high fidelity temperature and volumetric expansion data through this non-invasive approach. The quality of this data allows for further assessments as mechanical characteristics associated with dimensional changes of cells may indicate more than simple charging or discharging during cycling. While internal monitoring remains essential for future diagnostics, external monitoring using polymer fiber sensors offers a straightforward, superficial, and cost-effective sensing solution that opens a new avenue for real-time cell assessment, prognostics, and packaging considerations.
 [DOI: 10.1149/1945-7111/ac957e]

Manuscript submitted July 12, 2022; revised manuscript received September 13, 2022. Published October 10, 2022.

Supplementary material for this article is available online

The rapid growth and uptake of electrochemical energy storage devices have bolstered the importance of predictability across nearly all industries and applications. Indeed, the sustainability of lithium-ion batteries may well depend on the implementation of monitoring and sensing devices that can accurately identify metrics of interest as cells are put into use.[1] Of particular significance are thermodynamic parameters such as temperature,[2,3] pressure,[4,5] and strain,[6,7] which are known to allow for identification and discrimination of normal and parasitic reactions during charging and discharging and are also essential to auxiliary heating, cooling and safety systems (needed for many large battery packs).[8]

For the most part, temperature measurements are still relatively imprecise, with data generated at the pack level being optimized for cooling and thermal management, as opposed to being generated at the cell level for higher-order assessments.[8] Ideally, localized temperature data from cells could be used in conjunction with electrical metrics (e.g. voltage or resistance) in the battery management system (BMS) unit to optimize module- or pack- longevity, but existing temperature monitoring is ill suited for integration at this level. Nevertheless, different strategies exist for quantifying the internal and external thermal evolution of cells, including direct measurements of the cell thermal events (contact or contactless sensors), calorimetry,[9] and data-driven estimation models.[8,10,11] If precise and accurate temperature information were available, smart BMS systems utilizing heat generation models, heat transfer models, and machine learning could benefit significantly.[11]

Pressure measurements necessitate significant package modification, an invasive approach, or an unconventional environment. In perhaps the simplest form, one can note the cell design for any conventional Li-ion battery which has a built-in venting mechanism to prevent excessive pressure build-up. While this safety feature has undoubtedly prevented numerous incidents, the expendable and commoditized nature of these primary cells limits further investments. On the other hand, the life-cycle costs of current and future lithium-ion (and sodium-ion) batteries warrants exploration of increasingly intricate approaches which may also couple gas sensing with pressure measurements. Demonstrations of such approaches abound with custom cells,[12] and modified commercial designs,[13] but intrinsic challenges remain to scaling and widespread integration.[14]

For sealed systems like batteries, measurements of external strain are an attractive alternative to sensing internal pressure since they are derived from the volumetric expansion of the cells themselves, without the need for package modification. This can allow for direct observation of pressure-related events, such as internal gas build up, or purely mechanical artifacts such as electrode stack expansion/contraction during cycling. Although these expansion-causing events will happen concurrently, precision measurements of package

[=]Equal Contribution.
*Electrochemical Society Member.
[z]E-mail: julien.bonefacino@college-de-france.fr; steven.boles@ntnu.no

Table I. FBGs sensitivities of POF and SMF.

Fibers	Temperature (pm °C^{-1})	Strain (pm $\mu\varepsilon^{-1}$)	Pressure (pm MPa^{-1})
Polymer optical fiber	−24.94	1.5	29.5
Silica optical fiber	9.6	0.8	−3.4

deformation (vis-à-vis strain) may allow for their deconvolution since the event precursors have different characteristics (i.e. potential windows, rate dependencies, etc). Indeed, the importance of observing package expansion has been tried in many forms including dilatometry,[15–17] digital image correlation,[18] piezosensors,[19] strain gauges,[6] and others.[20] Looking ahead, strain measurements are slated to be essential for use in the monitoring of future solid-state batteries which have no fluids in their interior, and preliminary reports of such efforts are very encouraging thus far.[21,22]

Optical fiber sensors utilizing fiber Bragg gratings (FBGs) present an appealing unified monitoring solution for observing temperature, pressure, and strain. The low-cost, scalability, and compatibility with electrochemical energy storage devices and systems make them particularly well suited to filling the critical sensing gap which may unlock a new level of sustainability for Li- and Na-ion batteries.[1] The first proof of concept of temperature measurement of the anode and cathode of Li-ion coin cell using FBGs was presented by G. Yang et al..[23] The merits of FBG sensing in batteries were recognized by Nascimento et al.[24–26] who realized in-operando thermal measurements. The same group also demonstrated that FBGs harvest thermal signal with about 1.2 times higher response rate than thermocouples.[27] At the same time, Fleming et al. have shown in-operando distributed temperature sensing inside cylindric cells[28] and later Alcock et al. probed the external surface temperatures of 18650 cells.[29]

Strain measurements based on FBGs have also been investigated and the prescient work by Sommer et al. demonstrated that FBGs bonded on the package of a pouch cell can allow for monitoring of the strain generated by the electrode volume expansion upon lithiation.[30] Bae et al. took this work one step further by embedding FBGs sensors on top and inside the electrode to directly measure the anode volume expansion.[31] More recently, Peng et al. developed a device allowing to enhance the FBG-based strain sensor sensitivity and apply it for external strain measurement on a pouch cell.[32] The device permits sensitivity improvement by 11.69 times compared to a bare FBG sensor, but with the cost of a sizeable system. The value of FBG strain data was explored by Li et al. who demonstrated that the strain amplitude of FBG measured at the surface of a pouch cell could be linked to the battery capacity.[33]A more rigorous overview of the different fiber optic sensors explored with batteries can be found in the review by Han et al.[34]

While the observation of a single parameter certainly has value, simultaneous observations of multiple thermodynamic parameters allow for improved understanding of the origins and implications of (electro-)chemical events inside the battery upon cycling. For example, a recent demonstration by Huang et al.[35] highlights how combined pressure and temperature measurements from FBG sensors can be used to track the growth and evolution of the solid electrolyte interphase (SEI) in commercial 18650 cells. However, despite the high-value information generated through this type of approach, the delicate nature of physically inserting sensors into cell may slow their integration in products and systems.

Aside from devices made in standard silica-based optical fibers, FBGs can also be inscribed in polymer optical fibers (POF) made from commercially available cyclo-olefin polymer (ZEONEX®) granules. With drawing temperatures of less than ∼220 °C and FBG inscription times of 60 ns, POF FBGs have notable commercial advantages as they can be cheap and easy to manufacture. Although not explicitly utilized in the experiments here, the flexibility of a POF also translates into a bending radius of 2.5 mm for a 160 μm diameter fiber, opening up a wealth of opportunities for device and system integration. Importantly, the direction of wavelength shifting in POFs with respect to temperature, strain, and pressure, differ significantly from traditional silica optical fibers (Table I). For readers unfamiliar with how POFs compare with standard silica single mode fibers (SMFs), further commentary on their nature, are provided in the Supplementary Information, section 1.

In this work, POF FBGs are deployed in tandem with traditional FBGs inscribed silica and the pairs are affixed together to one side of the external surface of various battery packages. Wavelength shift signals from the FBGs are then decoded and transformed into strain and temperature shifts. The high-fidelity of the data generated from the POFs may open an exciting new path for sensing of packaged cells as both gassing and regular charge-discharge behavior are identified, and the merits of utilizing POF-FBGs are explored herein.

Experimental

Sensor design and sensing methodology.—Previous studies have demonstrated the use of silica-based FBG to monitor either the strain or the temperature changes of cells during the charge/discharge process.[25,26,28,32] In our experiments, the first fiber is a commercial germanium doped silica singlemode G657.B fiber (obtained from Silitec Fibers SA, Boudry, Switzerland), very similar to the one used in previous reports.[23,35–37] The second fiber, however, is a polymer optical fiber made of ZEONEX® (ZEON CORPORATION, Tokyo, Japan) with a core and cladding diameter of 9.3 μm and 160 μm, respectively. Such type of polymeric fiber exhibits much higher sensitivities than their silica counterpart due to their low Young modulus.[38] Detailed information regarding POF fabrication can be found in the work by X. Cheng et al.[39] and in the Supplementary Information. In our study, 3-mm FBGs were inscribed in both silica and POF using the phase-mask technic using an excimer laser at 248 nm (Braggstar M, Coherent Inc., Santa Clara, CA, USA) and their spectra is shown in Fig. 1a. Further information regarding the FBGs fabrication can be found in Supplementary information, section 2. Those FBGs exhibit thermal responses of −24.94 pm °C^{-1} for POF (Fig. 1b) and 9.62 pm °C^{-1} for SMF (inset of Fig. 1b). Moreover, not only does POF exhibit a sensitivity two times superior to SMF fiber for temperature measurements, but the coefficient is negative. Note that although the calibration of the POF sensor was performed at lower temperature in this case, it is relevant to emphasize that such sensors could be used reliably at higher temperature up to 110°C.[40] Furthermore, POF exhibit a higher strain sensitivity of 1.52 pm $\mu\varepsilon$ (Fig. 1c) compared to 0.839 pm $\mu\varepsilon^{-1}$ for SMF (inset of Fig. 1c). Due to its intrinsic properties, POF was tested at much higher elongation than SMF (five times more), which is undoubtably a considerable asset, enabling potential applications across a wide range of devices (and not just batteries). This renders the decoupling of strain and temperature events very trivial using a decoupling method with similar approach as shown by Huang et al.[35] and detailed in Supplementary Information section 3.

As both thermal and strain events shall be recorded, the package of the cell shall remain free to allow expansion, and therefore could not be clamped using conventional clamping fixtures commonly found on commercial batteries cyclers. Instead, 3D models of a cell holder made of Polylactic Acid (PLA) were designed using Solidworks® (Dassault Systèmes, France) and 3D-printed using I3-Mega (ANYCUBIC, MAYLERESCAPE Ltd., UK) as shown on Figs. 1d and 1e. To connect the cycler to the cell, copper foils were

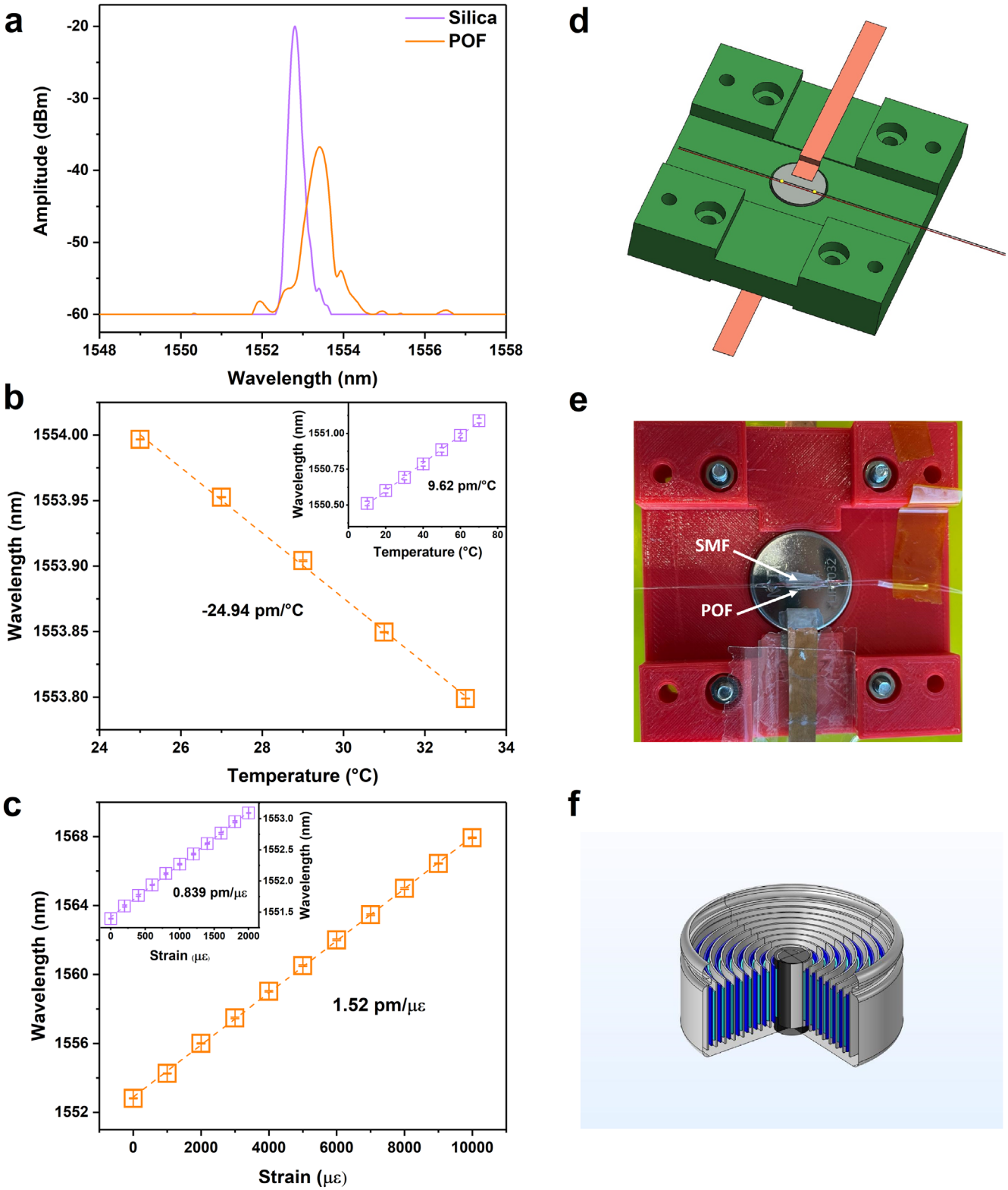

Figure 1. (a) POF and SMF FBG spectra. (b) Thermal sensitivity of the POF and SMF (inset). (c) Strain sensitivity of the POF and SMF (inset). (d) 3D design of the proposed test protocol. (e) Close view of the real set up, and (f) Schematic of the jelly roll 1258 button cell.

silver painted on the anode and cathode and secured by the 3D-printed cell holder (Fig. 1e).

The impact of the silver paint and the copper foil were investigated, and no difference was seen on the capacity or ohmic loss, as compared to a classical clamping method. For our proposed testing protocol, both the SMF and POF were placed close to each other on the package side of the electrode to be investigated and glued using epoxy (EPO-TEK® 301, EPOXY TECHNOLOGY, INC, BILLERICA, MA, USA) and let to cure overnight. The FBGs signals were recorded using optical interrogator Hyperion si155 (LUNA Inc., Roanoke, VA, USA), which has an accuracy limit of 1 pm shift. Thermal paste (STARS-612, Balance Stars) was applied

Table II. Thermal sensitivities recorded during the calibration of the investigated cells.

	Thermal sensitivity of glued SMF (pm °C^{-1})	Thermal sensitivity of glued POF (pm °C^{-1})
Unglued fibers	9.62	−24.94
Graphite anode cell	18.58	−91.43
SiO_x/C anode cell	24.58	−85.09
Prelithiated LTO	26.18	−75.38
Unprelithiated LTO	26.59	−76.21
LFP	14.43	−71.08

on the battery casing prior to placement of the fibers to allow better heat transfer during the cycling of the cells. As the fibers were slightly pre-strained during the curing of the epoxy, the thermal sensitivity of both the SMF and POF increased,[37] and thus, a thermal calibration was performed with the sensors glued on the cell prior to the battery cycling experiments. The calibration was performed within a range of 25 °C to 33 °C to avoid any deleterious effect on the electrolyte. Also note that the sensitivity to strain was established before the experiments (see Fig. 1c) and remains unchanged during the tests. A summary of the thermal sensitivities recorded for the sensors glued to all the investigated cells is summarized in Table II. lastly, we would like to affirm the fact that the sensor can be easily removed from the cell post-experiment, without provoking any damage to the cell package and the cell cyclability.

For all the tests performed, the testing units (battery holders, batteries, and FBGs) were placed in an environmental chamber (Espec SH-641, Osaka, Japan) with temperature set at 25 °C and humidity set at 65%RH for testing. The electrochemical data were recorded using Vertex.One.EIS (Ivium Technologies, Eindhoven, The Netherlands) and VMP-300 Potentiostat (BioLogic, Seyssinet-Pariset, France) battery cyclers.

Lithium-titanium-oxide (LTO) and lithium iron phosphate (LFP) cell preparations.—To fabricate the LTO-LTO symmetric- and LTO-LFP full-cells, commercial LTO (NANOMYTE® BE-10E (LTO)) and LFP sheets were purchased from NEI corporation (NANOMYTE® BE-60E (LFP)). The specifications of the procured electrodes are summarized in Table III. For coin cell assembly, disks of 12 mm diameter were punched out and paired in a coin-type cell (CR2025) using a 20 μm-thick porous polymer separator (Celgard, USA) and an electrolyte solution consisting of 1 M $LiPF_6$ in ethylene carbonate and ethyl methyl carbonate (EC:EMC, 3:7 v/v) (LB-005, DodoChem, China). The LTO-LTO symmetric cells were cycled at 0.2C in the potential windows of ±0.1 and ±0.2 V, with one LTO electrode being pre-lithiated before assembly. The LTO-LFP (N/P = 1) cells were operated at 0.2C, 0.4C, and 0.6C in the potential window of 1–2.5 V. The cells were rested at open circuit potential for roughly 48 h before cycling.

Results and Discussion

Demonstration using commercial 1258 button cell.—To demonstrate how polymer optical fiber sensors (POF-FBGs) can track the strain and temperature evolution in commercial batteries, two 1258 button cells were tested (provided by GP Batteries), each with chemically identical cathodes, but different anode compositions.

The first type is composed of a graphite anode and a $LiCoO_2$ (LCO) cathode, demonstrating a rated capacity of 60 mAh. The second type is composed of a blended SiO_x/C anode (approximate SiO_x content of over 10%) and an LCO cathode, with a rated capacity of 64 mAh. The exact formulations of the electrolytes for these cells are proprietary, but they are known to be based on $LiPF_6$ salts dissolved in carbonate-based solvents, as is commonly used in Li-ion rechargeable batteries. All GP cells have a jelly roll configuration and were provided with the SEI formation cycle already completed. A schematic of the 1258 cell with its jelly roll electrode configuration is shown in Fig. 1f. It is worth noting that the same set up was employed as shown in Fig. 1e, apart from the 3D-printed mold that was re-designed to accommodate the smaller button cell.

The sensors are implemented on 1258 cells having diameters of 12 mm, bearing in mind that this task should be easier on larger cells. Moreover, the two cells investigated have two different anode compositions, which permits identification of how the SiO_x addition contributes to the strain and thermal changes by comparing the two cells' behavior during cycling. Both cells were cycled according to the conditions which were provided by the manufacturer and are listed in the Supplementary Information (Section 4, Table SI). The schematic of the 1258 cell (Fig. 1f) shows that the bottom of the cell casing is slightly closer to the jelly roll structure than the top casing, which is the reason that the bottom side of the cell was used for affixing the fibers.

Figures 2a and 2b below show the thermal and strain data decoupled from the wavelength shift recorded for the second and third cycles for the LCO-graphite and LCO-SiO_x/C, respectively. The excellent repeatability of the measurements for both cells can be seen in Fig. 2a with five distinct thermal peaks (denoted "i_c," and "ii_c" during charge, and "i_d," "ii_d," and "iii_d" during discharge) regularly appearing during charge/discharge of the graphite-anode cell. In the case of the SiO_x/C-anode cell (Fig. 2b), at first glance we observed that the thermal events are very similar, but of greater magnitude. It can also be seen that some thermal peaks are evolving over these few cycles. More information and analysis of these thermal events can be found in the Supplementary Information (Section 5, Fig. S1, available online at stacks.iop.org/JES/169/100508/mmedia.).

The strain response of the POF-FBG (red curves in Figs. 2a and 2b) shows that the cell packaging experiences repeatable expansion/contraction during the lithiation/de-lithiation stages with maximum strain values of ∼100 $\mu\varepsilon$ and ∼170 $\mu\varepsilon$ for graphite and SiO_x/C anode cells, respectively, at the end of charge. In both cases, the signal appears to be highly reversible and with minor hysteresis to a null value at the end of discharge. This represents a lateral cell package volume expansion of only ∼0.01% (10,000 $\mu\varepsilon$ = 1%). Furthermore, a significantly higher strain was observed in the cell with SiO_x/C anode than with graphite anode, which matches with the expectation that the lithiation of Si, although diluted, contributes to a significantly increased volume expansion at the package level.

Direct comparison between the two cells is shown in Fig. 2c (temperature) and Fig. 2d (strain) recorded from the third cycle. The thermal response recorded for the two cells during charge and discharge clearly shows noticeably more heat generated in the SiO_x/C anode cell compared with the graphite one. The similar shapes of temperature profiles for the cells with SiO_x/C anodes and graphite anodes, both with the same LCO cathodes, might indicate that the thermal fluctuations likely arise from the reactions at the cathodes. The significantly different amplitude of the temperature profile, especially at the state of charge (SOC) above 10%, could possibly hint that high stress changes due to SiO_x/C anode expansion and contraction might alter the thermal dissipation inside the cells.

In Fig. 2d, the strain curves for the graphite and SiO_x/C-anode cells exhibit clear differences. Despite the total magnitude of strain (i.e. package expansion) being nearly double for the SiO_x/C, both strain curves for the two anode types show relatively smooth and consistent evolution during charge (anode lithiation), suggesting that

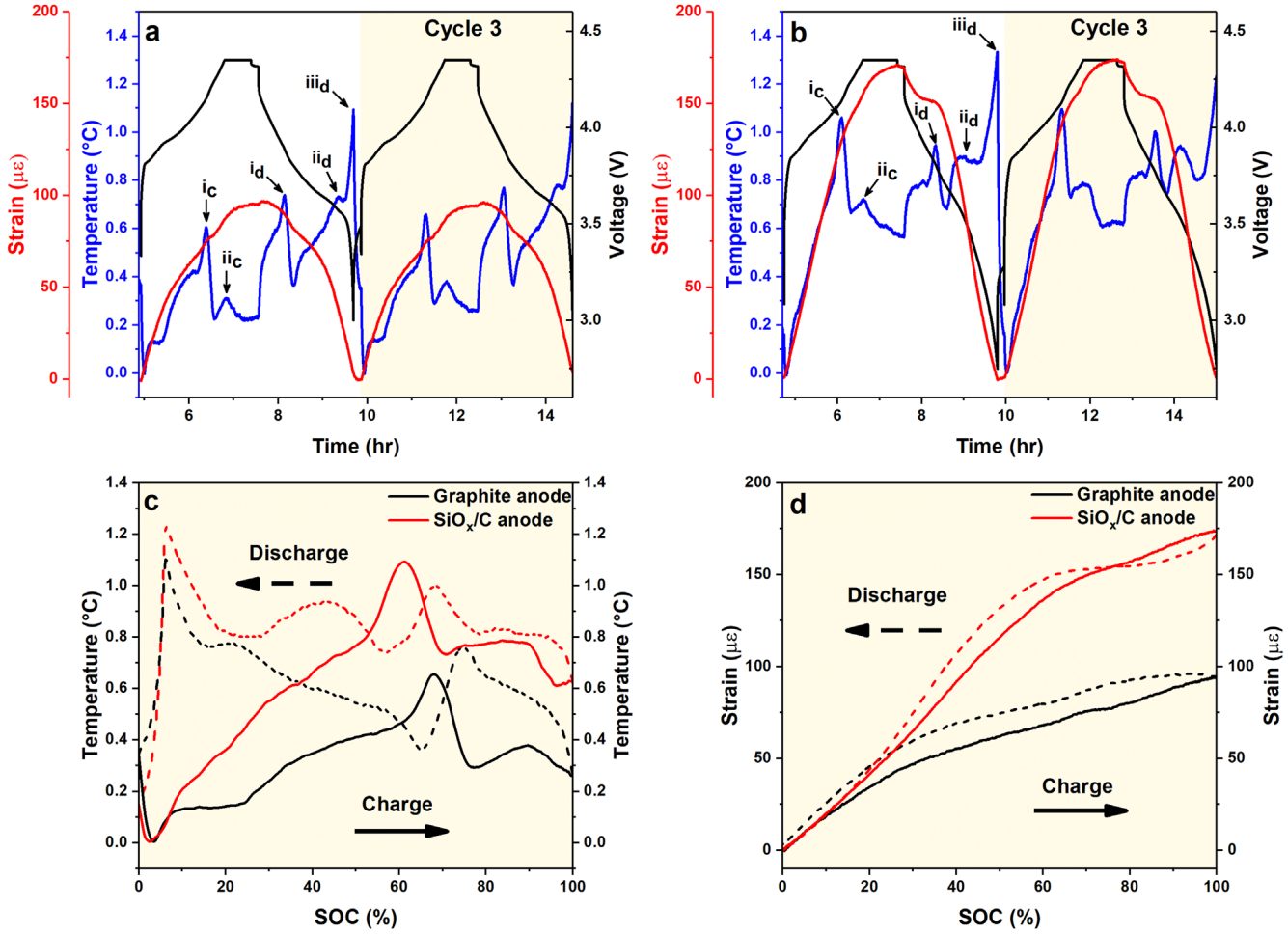

Figure 2. (a) Temperature and strain response recorded during the second and third cycles for the graphite anode battery. (b) Temperature and strain response recorded during the second and third cycles for the SiO_x/C anode battery. (c) Comparison of the thermal fluctuations in function of the state of charge (solid lines) and discharge (dashed lines) for the graphite anode cell (black) and SiO_x/C anode cell (red) for the third cycle. (d) Comparison of the strain fluctuations in function of the state of charge (solid lines) and discharge (dashed lines) for the graphite anode cell (black) and SiO_x/C anode cell (red) for the third cycle.

Table III. The specifications of LFP and LTO composite electrodes.

Electrodes	Average particle size (μm)	Current collector	Electrode coating components and content (%)	Active material areal loading (mg cm^{-2})
$Li_4Ti_5O_{12}$	~2	Copper foil	LTO: Carbon Black: Binder (90:5:5)	7.3 ± 5%
$LiFePO_4$	1.5–3	Aluminum foil	LFP: Carbon Black: Binder (90:5:5)	7.3 ± 5%

lithiation occurs almost simultaneously into both SiO_x and graphite materials, although hints of minor slope changes may be noted at ~60% SOC for SiO_x/C and ~25% SOC for graphite. However, during discharging (and anode delithiation), a pronounced two-stage evolution was observed in the strain curve for the SiO_x/C cell, consistent with previous observations of mixed graphite-silicon material blends using *operando* energy dispersive X-ray diffraction.[41]

From the preliminary investigations reported here, the combination of the POF FBG and classic silica FBG offer valuable insights for battery developers and manufacturers due to the high sensitivity of our POF. Decoupled strain and temperature measurements can give evidence of phenomena associated with anode and cathode chemistries, as demonstrated here with the significant increase in package strain stemming from a small addition of SiO_x to the anode and a ~7% increase in capacity. Despite the ambiguity of the measurement (i.e. due to the jelly roll structure of the cell), the FBGs are measuring the overall volume changes taking into account all cell components.

After demonstrating this method with commercial LIB cells, we extend POF sensing to non-commercial battery cells assembled in the laboratory, with 2025-coin cells, in an effort to establish the sensitivity limits for superficial measurements of batteries with POFs. By properly selecting the nature of the counter electrode (e.g. zero-strain $Li_4Ti_5O_{12}$ electrode), we can solely access the thermal/mechanical events of various positive electrode chemistries.

LTO-LTO symmetric cells.—$Li_4Ti_5O_{12}$ (LTO) has long been a popular anode material for Li-ion batteries and was successfully commercialized for EV applications, e.g., Toshiba SCiB^{TM} cells. LTO is used as a high potential anode material (with a redox potential at ~1.55 V vs Li/Li$^+$),[42] which endows Li with the

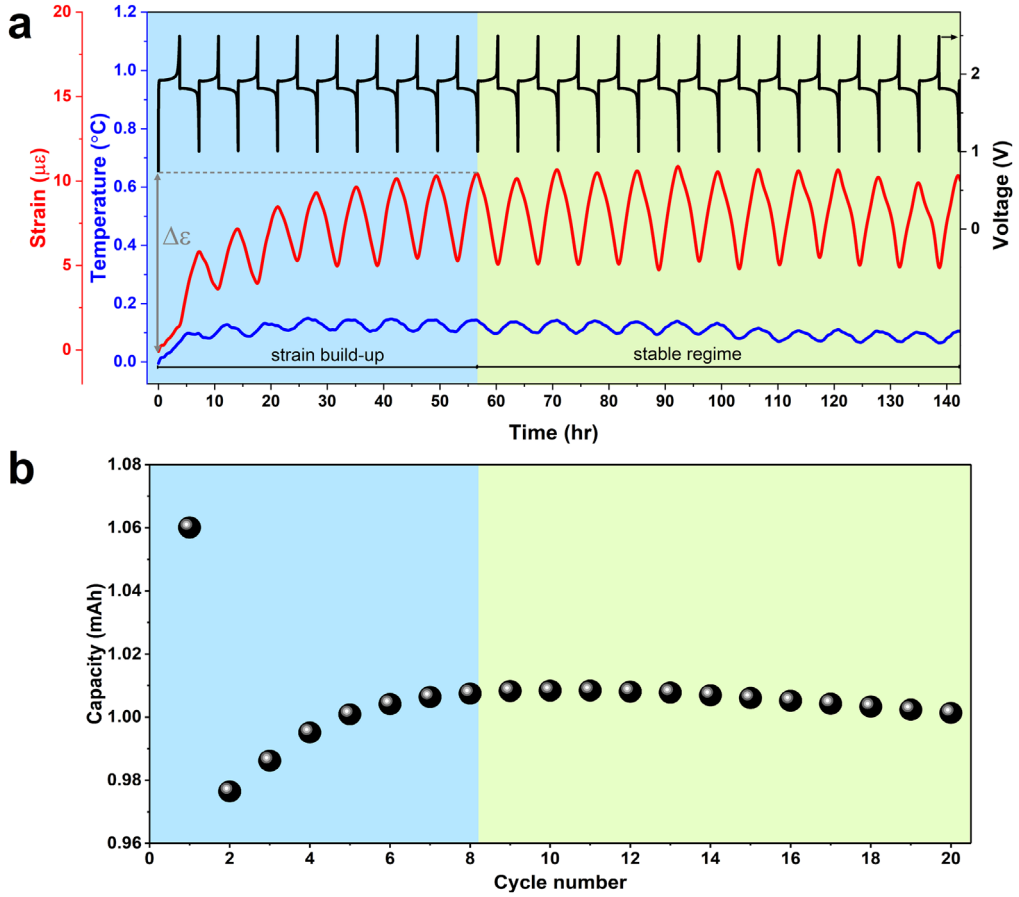

Figure 3. (a) Strain evolution in conjunction with galvanostatic voltage profile for the LFP-LTO cell cycled at 0.2C after decoupling the *operando* FBG wavelength shift data. (b) Charge capacity in function of the cycle number during the first test at 0.2C.

high level of safety by inhibiting Li plating and dendrite formation as well as mitigating electrolyte reduction reactions. Not only does LTO benefit from its SEI-free nature and high-rate capability, but the spinel structure is also known to exhibit "zero-strain" upon lithiation-delithiation, such that superior mechanical stability and a remarkable long-term performance of the electrode can be ensured.[43] By taking advantage of the above-mentioned features as numerous groups have done,[21,42,44] LTO can potentially serve as a counter electrode in our FBG tests, with sensor reading stemming solely from the working electrode.

The details of this work are shared in the Supporting Information, section 6, and are consistent with others[21,44] who have utilized LTO for non-FBG based volume expansion experiments. Noteworthy to mention that in the case of symmetric LTO/LTO cells, our external FBG sensor pairs are not sensitive enough to capture strain evolving during the phase transformation (Figs. S2 and S3). As for the temperature profile, cells do not show correlation with voltage or time, indicating that the LTO in our system does not contribute to significant thermal changes (Fig. S4). Therefore, so long as the phase transformation of LTO is utilized exclusively,[45] the FBG sensing data will allow us to exclude this electrode from any thermal or mechanical phenomena observed.

LFP-LTO full cell.—$LiFePO_4$ (LFP) is a favored cathode material for a variety of applications due to its general reliability and safety. In this work, it was selected as the working cathode owing to its relatively small volume change of around 6.7% during lithium insertion/extraction[20] and good thermal stability, making it ideal for benchmarking the capabilities of the POF-FBG externally affixed sensing method.

Figure 3a shows the potential evolution along with the strain and temperature variations with respect to time for the first twenty cycles of the LFP-LTO cell with 0.2C galvanostatic constant discharge (GCD) cycling. It can be clearly seen that both the strain and temperature changes experienced by the sensor evolves continuously in response to changes in the cell's volumetric evolution and heat generation during repeated charge/discharge cycles, which can safely be attributed to the insertion/extraction of Li^+ into/from LFP electrode. The seemingly linear dependence of stress and strain on Li^+ concentration during electrochemical cycling of LFP has been reported using in situ techniques including the curvature measurement method[20] as well as the digital image correlation (DIC) technique.[46] The temperature changes recorded by the sensor also consistently track small, but real fluctuations (less than 0.1 °C) attributed to insertion/extraction of Li^+ into/from LFP electrode.

The precision of the strain and temperature measurements also showcase the outstanding sensitivity of the fibers. While Özdogru et al.[46] reported an expansion of around 0.6% at an electrode level upon the first lithiation of a self-standing LFP composite cathode using the DIC technique, here the FBG sensors captured a lateral whole-cell expansion of 0.0003%–0.0005% upon Li-ion insertion into LFP at 0.2C. This indicates the remarkably high fidelity of the optical fiber sensors to respond to the minute volumetric changes at the package level during electrochemical cycling.

Highlighted in blue in Fig. 3a, a build-up of strain is observed during the first eight cycles, indicating an irreversible cell expansion while the amplitude of the Li-driven strain between charge and discharge is also increasing up to the 8 cycles. Noteworthy, this increase corresponds to an increase in cell charge capacity retention upon cycling (Fig. 3b), quite consistent with the largest strain for the largest amount of Li^+ uptake or release. Usually, irreversible cell

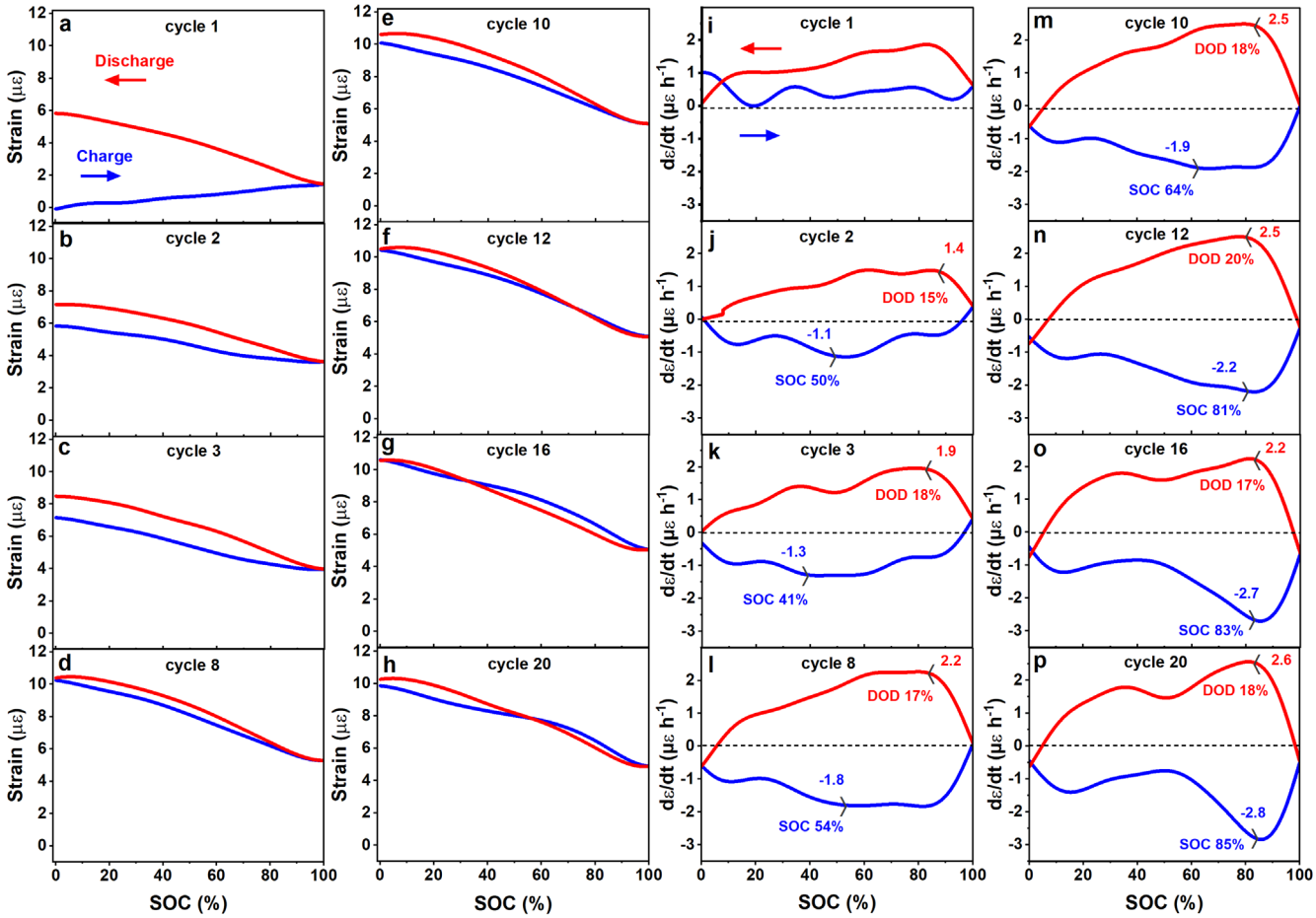

Figure 4. (a)–(h) The strain hysteresis loops for the LFP-LTO full cell in the first 20 cycles at 0.2C. The terms charge and discharge denote LFP delithiation and LFP lithiation, respectively. (i-p) Strain rate as a function of state of charge in the LFP-LTO full cell cycled at 0.2C. A smoothing function of Fast Fourier Transform (FFT) has been applied prior to the differentiation of strain over time.

expansion is attributed to the SEI formation and electrolyte breakdown at the anode. However, this is not feasible here since $Li_4Ti_5O_{12}$ is known as SEI-free insertion material. Therefore, we believe that the observed strain build-up can be nested in the oxidative decomposition of electrolyte on the LFP cathode during the formation of the cathode-electrolyte interphase (CEI), which is accompanied by the deposition of solid precipitates and release of gaseous species.[47,48] The onset of electrolyte oxidation is limited by the low operating potential of LFP and the contribution of CEI-related reactions to the total cell expansion is presumed to be smaller for LFP as compared to high-voltage cathode materials such as NMC.[49] Driven by the aforementioned factors, the coin cell expands continuously in the initial cycle, even during charge when the LFP is being delithiated. In the second cycle, however, the strain drops 2.3 $\mu\varepsilon$ during charge, while rising 3.6 $\mu\varepsilon$ upon the following discharge (LFP lithiation), showing a positive strain off-set of 1.3 $\mu\varepsilon$. This residual strain keeps building up for around eight cycles, before reaching a stable region (green zone in Fig. 3) where the volumetric changes of the cell package upon cycling are virtually reversible. Overall, the first few cycles of Fig. 3 are quite identical to the ones published elsewhere,[12] in which gas formation was identified as the major contributor to the irreversible pressure build-up of a lithium cell containing LTO electrode.[12]

Mechanical stabilization of the cell during the initial cycles can also be understood from the strain hysteresis loops shown by Figs. 4a–4h, as they become thinner and move towards more tensile values during the first eight cycles but remain virtually identical in size and strain values afterwards. As a complement to the absolute strain values, the rate at which the strain evolves during different cycles can also provide insights into the mechanical evolution of the package. Figures 4i–4p plot the evolution of strain rate vs SOC during each cycle where the loop-shaped profiles grow bigger over the first eight cycles. Cumulatively, this implies a gradual shift to higher rates of contraction/expansion. Herein, the thinnest loop is obtained at the first cycle (Fig. 4i), where both charge and discharge generate tensile strain due to the dominance of expansion-inducing reactions. From the second charge onwards, the strain rate during charge is evidenced by contraction (i.e. negative strain rate values), implying that the parasitic reactions such as gas formation become less dominant compared to the regular electrode material volumetric changes. Furthermore, the charge and discharge strain rate profiles become relatively symmetric with respect to the zero-strain dashed line, evident in the 8th and the following cycles (Figs. 4l–4p), suggesting cell stabilization due to the dominance of reversible cell reactions over the parasitic ones.

The strain rate is also of great importance in terms of the mechanical damage that the cell could be exposed to at high rates of contraction/expansion at a fixed C-rate. As marked by black arrows in Figs. 4j–4p, the magnitude of the maximum compressive strain rate increases from -1.1 $\mu\varepsilon$ h^{-1} in the second charge to -1.8 and -2.8 $\mu\varepsilon$ h^{-1} in the 8th and 20th charge, respectively, with the occurrence location (SOC) shifting from 45%–55% SOC in the first eight cycles to 85% SOC in the 20th cycle. Likewise, the maximum tensile strain rate rises from 1.4 $\mu\varepsilon$ h^{-1} in the second discharge to 2.2, and 2.5 $\mu\varepsilon$ h^{-1} in the 8th and 20th discharge, respectively, all occurring at 15%–20% DOD. Technically, an appropriate estimate of the strain rate evolution trajectory during each charging and discharging would enable battery management systems to optimize

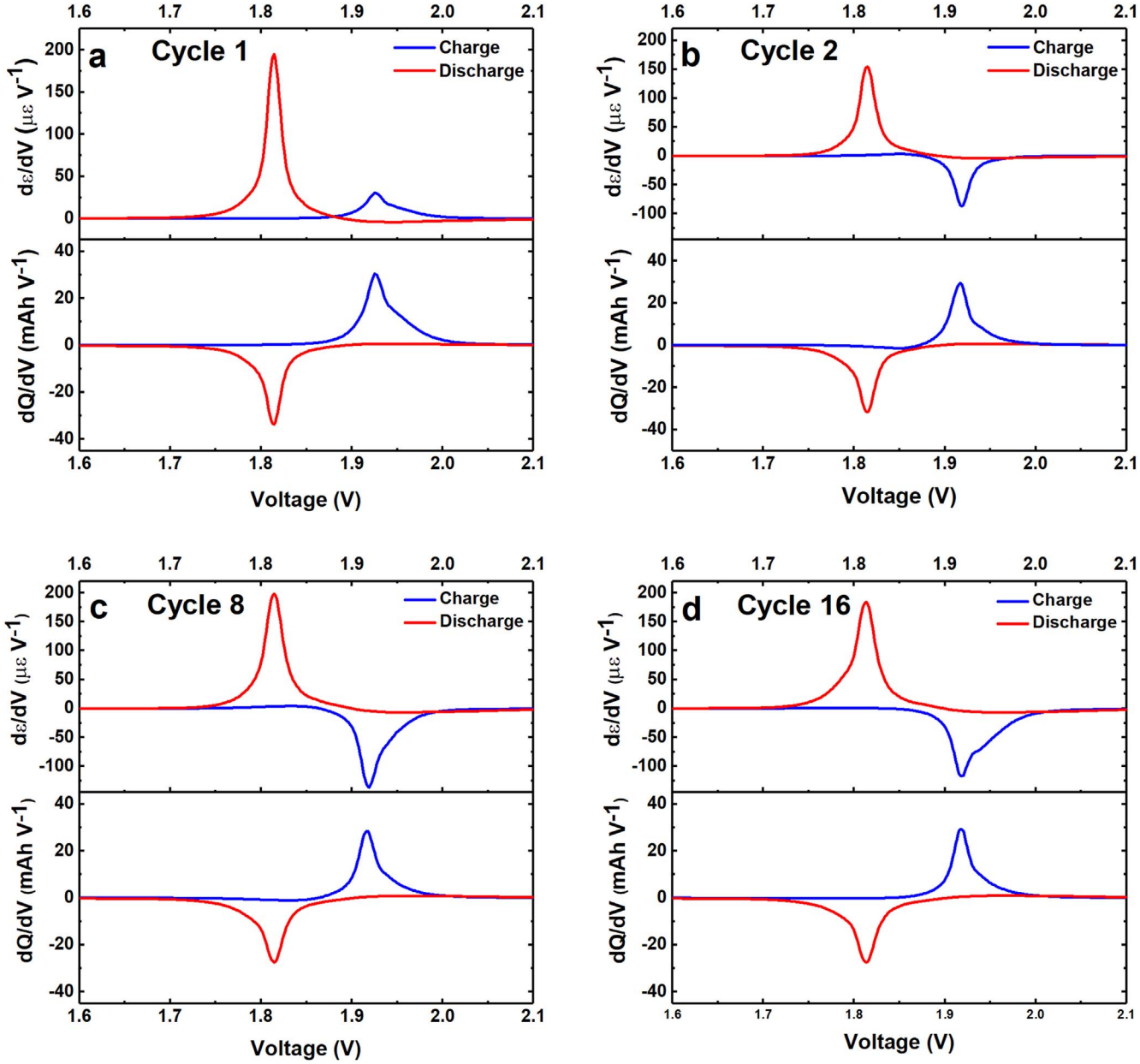

Figure 5. Differential strain—cell voltage (top) is plotted in conjunction with differential capacity—cell voltage (bottom) for (a) cycle 1, (b) cycle 2, (c) cycle 8, and (d) cycle 16. Note that the scale of (a) is different than the scale of (b), (c) and (d) for better visibility.

the rate of charge/discharge as the cell approaches high (i.e. predetermined) deformation rates in order to minimize possible damage to the electrode binder material, or the active material itself.

Incremental capacity analysis (ICA) vs incremental strain analysis (ISA).—In general, ICA differentiates the cell capacity over the cell potential (i.e., dQ/dV) during charge and discharge. Since the nature of Li-ion reactions involved at each electrode determines the total cell voltage, ICA provides for a non-invasive and in situ approach that can yield critical insights into cell performance, particularly over time. For example, *Dahn* et al. demonstrated that a battery's long-term behavior could be predicted using voltage slippage, as observed in dV/dQ curves.[50] Therefore, in a BMS, ICA can be used to estimate critical parameters, such as the state of health (SOH), and shed light on battery aging by identifying things such as capacity loss during operation.

Herein, the dQ/dV data is plotted in conjunction with dε/dV data generated by the FBG testing platform (Fig. 5) for cycles 1, 2, 8, and 16 from LFP-LTO cells. It should be noted that a moving regression called locally weighted scatterplot smoothing (LOWESS) is applied to smooth the FBG data prior to differentiating the capacity and the strain. The conventional dQ/dV curves are presented in the lower halves of Figs. 5a–5d and despite the strain signal used here being harvested at the package level, the ISA clearly mirrors the results obtained with ICA. Interestingly, the amplitude of the dε/dV during charge exhibits fluctuations during the first initial cycles prior to stabilizing after the 8th cycle (Figs. 5a–5c). Noteworthy is the broadening of the signal dε/dV near the 16th cycles (Fig. 5d) that may reminiscent on the appearance of inhomogeneous strain distribution through the sample.

After characterizing the LFP-LTO cell which has a relatively stable chemistry, it is believed that our FBG testing platform can be extended to more complicated battery chemistries for testing scenarios where gas evolution and mechanical expansion might be more concerning. Additionally, our sensing technology could be used to enrich the understanding of other electrochemical energy

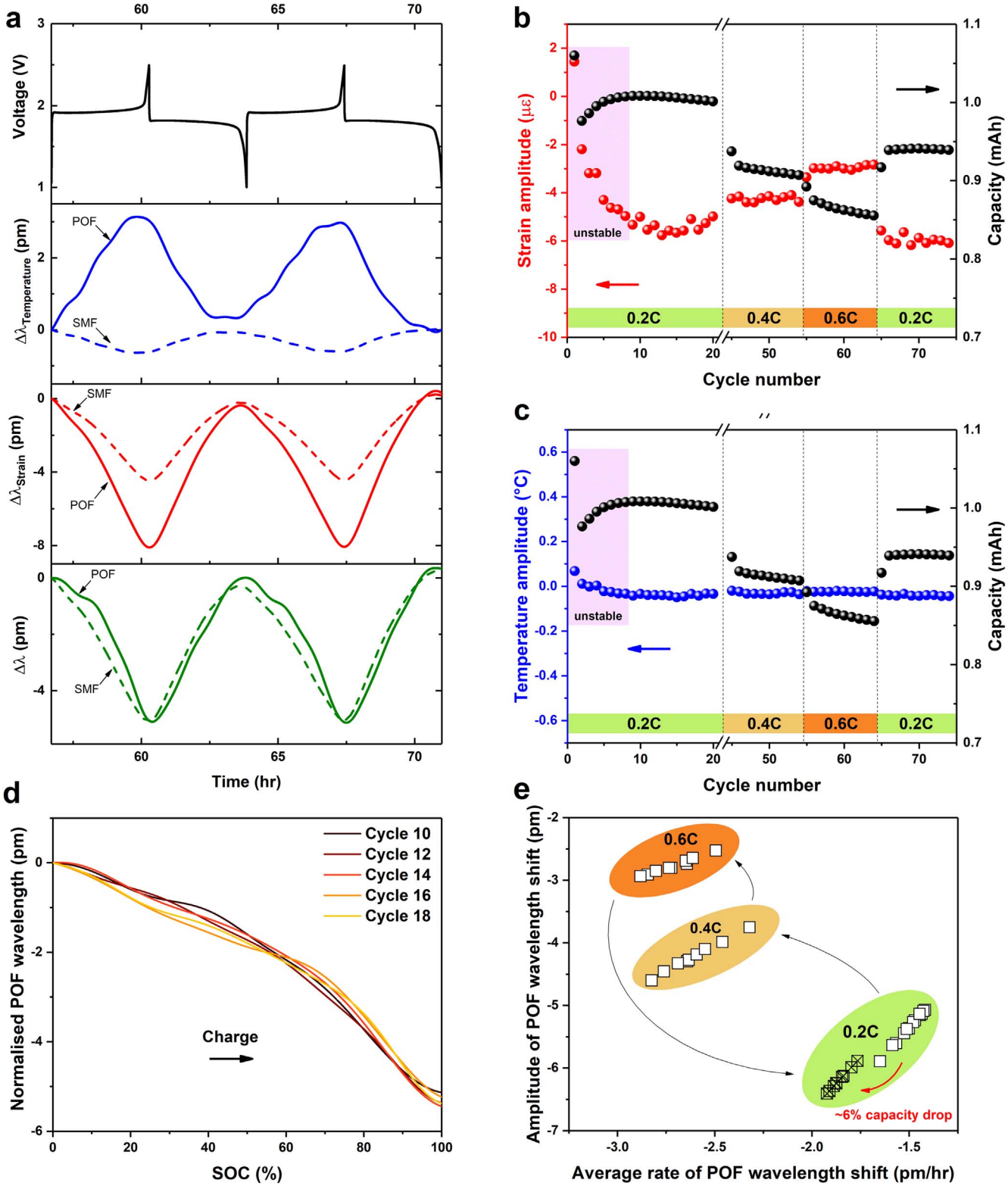

Figure 6. Monitoring temperature and strain in a $LiFePO_4/Li_4Ti_5O_{12}$ cell:(a) Voltage (top), wavelength shift experienced by the POF and SMF fibers induced by thermal effect (second row), wavelength shift experienced by the POF and SMF fibers induced by strain effect (third row), and cumulated temperature and strain-driven wavelength shift experienced by the POF and SMF fibers (bottom) during the 8th and 9th cycles (stable regime). (b) Decoupled strain amplitude and charge capacity in function of the cycle number. (c) Decoupled temperature amplitude and charge capacity in function of the cycle number. (d) Normalized POF wavelength shift in function of SOC once a stable cycling regime has been achieved. (e) The amplitude of the POF wavelength shift during cycling at different C-rates in function of the average rate of the POF wavelength shift during charge in the stable operational regime of the cell.

storage devices, such as supercapacitors or hybrid capacitors which have many structural similarities with respect to assembly and packaging.

Potential for using a single POF fiber.—In the past few years, different methods have been proposed to estimate the SOC of cells using FBGs. A first approach was to assess SOC using FBG strain

induced at the package level.[32,36,37] While each of these works represents notable progress in the field, the decoupling approaches for mechanical and thermal events are problematic because they do not account for the strain associated with thermal expansion of the cell, and thus lack critical information regarding the dynamic exo-/endothermic chemical reactions inside each cell, as these will naturally impact the quantified strain data. Others have sought to embed the FBG in pouch cells at the electrode level, which can allow for monitoring the SOC as well as the SOH.[51,52] In all configurations used here, the authors show a correlation between the wavelength shift and "stress" measured by the FBGs with the SOC, but their stress value is intrinsically convoluted with temperature. More recently, this method was enhanced by Albero Blanquer et al. with an extension to solid state anodes,[53] which revealed hidden mechanical changes in the electrodes that could not be observed with external force sensing. Nevertheless, while this method certainly is promising, it is an *operando* measurement at the electrode level requiring irreversible modifications for preparation and processing.

Interestingly, the inverse nature of the thermal and strain response coefficients of POFs, together with their intrinsic larger sensitivities, may break a critical limitation of SMFs in decoding the nature of internal events, since in the former case they are positive and negative, respectively, whereas with the latter they are both positive. For example, Fig. 6a shows the voltage profile (top row), together with the wavelength shift attributed to thermal effect (second row, in blue) and strain effect (third row, in red) experienced by the POF and the SMF fibers during the 9th and 10th cycle of a $LiFePO_4/Li_4Ti_5O_{12}$ cell at 0.2C. It is evident that the POF yields appreciably more information than its silica counterpart (Fig. 6a). Indeed, the contributions to the wavelength shift from temperature and strain are significantly greater in magnitude for the POF compared to the SMF. Interestingly, the net wavelength shifts (bottom, green) are very similar for both the POF and SMF due to their nature (+/−, +/+). The observed similar amplitude of the cumulative $\Delta\lambda$ is purely coincidental, but there is no reason for this to be. We should note here that in these experiments, the fibers were glued with epoxy and thermal paste was applied beneath the fiber to maximize thermal contributions. However, thermal isolation strategies can readily be envisioned which would dampen and minimize such contributions to the net wavelength change.

By taking the maximum strain and temperature amplitudes during full charging and comparing it to the capacity, useful information may be harvested as shown in Figs. 6b and 6c. For example, the changes in the cell charge capacity during the first eight cycles (unstable regime) can be readily identified using the strain amplitude metric (Fig. 6b). Indeed, it is seen in Fig. 6b that the strain amplitude and capacity of the cell appear to be related, as the link between capacity and C-rate provides a stimulus for such an observation (see also Fig. S5). Moreover, Fig. 6c shows that virtually no heat is generated by the cell other than during the first cycle, regardless of C-rate (again in Fig. S5). Therefore, the main contributor to the POF wavelength shift within the cycling conditions used is the strain as hinted in Fig. 6a. These observations suggest the opportunity to use a single POF to monitor a cell as it is reasonable to expect that if strain can be used for SOC estimation,[37] then the raw data generated by a single POF may also indicate SOC. Driving this idea forward, we can see in Fig. 6d that the normalized POF wavelength shift taken during the stable operational regime of the cell could be a simple and straightforward method to access the SOC/DOD with a quasi-linear correlation. Indeed here, no math is necessary, contrary to the method presented in Figs. 3b and 6b and 6c, that requires a second FBG and a calculation/matrix operation.

With relationships and correlations appearing between sensor data and electrochemical data, we briefly consider further prospects for these parallel information channels. For example, with the capacity related to the maximum wavelength shift amplitude (Fig. 6b), the C-rate might also be crudely approximated by average rate of change of the wavelength shift during a half-cycle. Therefore, similar to how C-rate and capacity information have been used to build degradation models,[54] this could allow for two-dimensions of *only* sensor data to capture a cell's condition, without input from the electrochemical system. An example of this is plotted in Fig. 6e, where a ~6% drop in capacity between the 0.2C groups is immediately evident in the discontinuity of these groups of data (open squares vs closed squares in green). Admittedly, this type of analysis becomes specific to charging protocols and cell chemistries, but nevertheless, these emerging operational and physical links are encouraging.

Further exploration of sensing data within each cycle opens up the exciting possibility of using a single fiber for SOH estimation, which has been a long-standing goal of fiber sensing in batteries, as already attempted by others. By comparing the derivative of the wavelength shift induced by the strain signal of the FBG and the ICA curve, Sommer et al. were somewhat successful in spotting phase transitions in graphite[36] and comparing dSOC/dV with $d\lambda/dV$. Analysis of dSOC/dV and dQ/dV have both been shown to be instructive for identifying a loss of lithium inventory, as well as incomplete anode lithiation, which are excellent indicators for the aging of lithium-ion batteries and their associated SOH.[55] However, the analysis of Sommer et al. relies on a wavelength shift due to the decoupled strain (requiring two fibers: one for measurement and one for thermal compensation), not the wavelength shift of a single FBG. Such analysis may be out of the scope of this manuscript, but the authors would like to direct the reader to the Supplementary Information sections 8 and 9, where it is proposed that a single POF could potentially be used for SOH estimation following the evidence of Liu et al.[55] who established connections between SOH and ICA. From the results disclosed here, the use of a single POF in a coin cell with a counter LTO electrode could possibly allow for monitoring SOC, monitoring of the lithiation stage and phase transformations of the electrode, and more generally assessing the SOH of the battery.

Conclusions

In this work, we have demonstrated how a POF fiber sensor can be used for superficial battery monitoring, either by pairing this POF-FBG with a standard SMF-FBG to accurately decouple thermal and strain events during charge/discharge, or through reliance on the single POF-FBG's improved sensitivity. With primary and parasitic phenomena, such as Li-ion insertion and gas formation, leading to different mechanical response patterns, sensing data may be either complementary or superior to assessments that rely on coulombic monitoring alone. The integration of a low cost POF sensor at the cell or pack level can be envisioned for real-time, on-line assessment for diagnostic or prognostic health management, or alternatively as a powerful tool for battery manufacturers to assess their cells and the associated characteristics arising from their materials and production methods.

Acknowledgments

This paper is supported by Centre for Advances in Reliability and Safety (CAiRS) admitted under AIR@InnoHK Research Cluster, the Hong Kong Research Grants Council project (PolyU 252166/17E), and the HK PolyU Postdoc Matching Fund Scheme (1-W14W). The authors are also thankful to GP batteries for the provision of the 1258 cells, to Dr X. Cheng from the department of Electrical Engineering of the Hong Kong Polytechnic University for the provision of the POF fibers, and particularly to Dennis Tsang at CAiRS for his administrative support and organization. SB acknowledges the support from the ENERSENSE research initiative (68024013) at the Norwegian University of Science and Technology (NTNU), Norway. JMT acknowledges funding from the International Balzan Prize Foundation.

ORCID

Julien Bonefacino https://orcid.org/0000-0001-5147-9873
Laura Albero Blanquer https://orcid.org/0000-0001-7906-4442
Steven T. Boles https://orcid.org/0000-0003-1422-5529

References

1. J. Huang, S. T. Boles, and J.-M. Tarascon, *Nat Sustain*, **5**, 194 (2022).
2. K. M. Carthy, H. Gullapalli, and T. Kennedy, *J. Power Sources*, **519**, 230786 (2022).
3. S. Zhu, J. Han, T.-S. Pan, Y.-M. Wei, W.-L. Song, H.-S. Chen, and D. Fang, *Extreme Mechanics Letters*, **37**, 100707 (2020).
4. S. Zhu, L. Yang, J. Fan, J. Wen, X. Feng, P. Zhou, F. Xie, J. Zhou, and Y.-N. Wang, *Journal of Energy Storage*, **42**, 103049 (2021).
5. R. Lundström and E. J. Berg, *J. Power Sources*, **485**, 229347 (2021).
6. S. Zhu, L. Yang, J. Wen, X. Feng, P. Zhou, F. Xie, J. Zhou, and Y.-N. Wang, *J. Power Sources*, **516**, 230669 (2021).
7. H. Xie, B. Han, H. Song, X. Li, Y. Kang, and Q. Zhang, *J. Mech. Phys. Solids*, **156**, 104602 (2021).
8. A. Jinasena, L. Spitthoff, M. S. Wahl, J. J. Lamb, P. R. Shearing, A. H. Strømman, and O. S. Burheim, *Front. Chem. Eng.*, **4**, 804704 (2022).
9. L. J. Krause, L. D. Jensen, and J. R. Dahn, *J. Electrochem. Soc.*, **159**, A937 (2012).
10. L. H. J. Raijmakers, D. L. Danilov, R.-A. Eichel, and P. H. L. Notten, *Appl. Energy*, **240**, 918 (2019).
11. A. Samanta and S. S. Williamson, *Energies*, **14**, 5960 (2021).
12. A. Schiele, T. Hatsukade, B. B. Berkes, P. Hartmann, T. Brezesinski, and J. Janek, *Anal. Chem.*, **89**, 8122 (2017).
13. M.-S. Park, J.-W. Lee, W. Choi, D. Im, S.-G. Doo, and K.-S. Park, *J. Mater. Chem.*, **20**, 7208 (2010).
14. H. Li, S. Guo, and H. Zhou, *Journal of Energy Chemistry*, **59**, 191 (2021).
15. A. J. Louli, L. D. Ellis, and J. R. Dahn, *Joule*, **3**, 745 (2019).
16. P.-K. Lee, M. H. Tahmasebi, S. Ran, S. T. Boles, and D. Y. W. Yu, *Small*, **14**, 1802051 (2018).
17. H. Popp, M. Koller, M. Jahn, and A. Bergmann, *Journal of Energy Storage*, **32**, 101859 (2020).
18. P. K. Leung, C. Moreno, I. Masters, S. Hazra, B. Conde, M. R. Mohamed, R. J. Dashwood, and R. Bhagat, *J. Power Sources*, **271**, 82 (2014).
19. J. M. Kaule, L. R. Hoffman, and H. Mukaibo, *Anal. Methods*, **7**, 7256 (2015).
20. M. Janzen, D. Kramer, and R. Mönig, *Energy Technol.*, **9**, 2000867 (2021).
21. F. Strauss, D. Kitsche, Y. Ma, J. H. Teo, D. Goonetilleke, J. Janek, M. Bianchini, and T. Brezesinski, *Adv Energy Sustain Res*, **2**, 2100004 (2021).
22. S. Y. Han, C. Lee, J. A. Lewis, D. Yeh, Y. Liu, H.-W. Lee, and M. T. McDowell, *Joule*, **5**, 2450 (2021).
23. G. Yang, C. Leitão, Y. Li, J. L. Pinto, and X. Jiang, *Measurement*, **46**, 3166 (2013).
24. M. Nascimento, M. S. Ferreira, and J. L. Pinto, *Appl. Therm. Eng.*, **149**, 1236 (2019).
25. M. Nascimento, S. Novais, M. S. Ding, M. S. Ferreira, S. Koch, S. Passerini, and J. L. Pinto, *J. Power Sources*, **410–411**, 1 (2019).
26. M. Nascimento, M. Ferreira, and J. L. Pinto, *Batteries*, **4**, 23 (2018).
27. M. Nascimento, M. S. Ferreira, and J. L. Pinto, *Measurement*, **111**, 260 (2017).
28. J. Fleming, T. Amietszajew, E. McTurk, D. P. Towers, D. Greenwood, and R. Bhagat, *HardwareX*, **3**, 100 (2018).
29. K. M. Alcock, M. Grammel, A. González-Vila, L. Binetti, K. Goh, and L. S. M. Alwis, *Sens. Actuators, A*, **332**, 113061 (2021).
30. L. W. Sommer, P. Kiesel, A. Ganguli, A. Lochbaum, B. Saha, J. Schwartz, C.-J. Bae, M. Alamgir, and A. Raghavan, *J. Power Sources*, **296**, 46 (2015).
31. C.-J. Bae, A. Manandhar, P. Kiesel, and A. Raghavan, *Energy Technol.*, **4**, 851 (2016).
32. J. Peng, X. Zhou, S. Jia, Y. Jin, S. Xu, and J. Chen, *J. Power Sources*, **433**, 226692 (2019).
33. Y. Li, Y. Zhang, Z. Li, Z. Yan, X. Xiao, X. Liu, J. Chen, Y. Shen, Q. Sun, and Y. Huang, *Adv. Sci.*, **9**, 2203247 (2022).
34. G. Han, J. Yan, Z. Guo, D. Greenwood, J. Marco, and Y. Yu, *Renew. Sustain. Energy Rev.*, **150**, 111514 (2021).
35. J. Huang et al., *Nat. Energy*, **5**, 674 (2020).
36. L. W. Sommer, A. Raghavan, P. Kiesel, B. Saha, J. Schwartz, A. Lochbaum, A. Ganguli, C.-J. Bae, and M. Alamgir, *J. Electrochem. Soc.*, **162**, A2664 (2015).
37. B. Rente, M. Fabian, M. Vidakovic, X. Liu, X. Li, K. Li, T. Sun, and K. T. V. Grattan, *IEEE Sensors J.*, **21**, 1453 (2021).
38. J. Bonefacino, H.-Y. Tam, T. S. Glen, X. Cheng, C.-F. J. Pun, J. Wang, P.-H. Lee, M.-L. V. Tse, and S. T. Boles, *Light: Sci. Appl.*, **7**, 17161 (2018).
39. X. Cheng, D. S. Gunawardena, C.-F. J. Pun, J. Bonefacino, and H.-Y. Tam, *Opt. Express*, **28**, 33573 (2020).
40. D. S. Gunawardena, X. Cheng, J. Cui, G. Edbert, L. Lu, Y. T. Ho, and H.-T. Tam, *Photon. Res.*, **10**, 1011 (2022).
41. K. P. C. Yao, J. S. Okasinski, K. Kalaga, J. D. Almer, and D. P. Abraham, *Adv. Energy Mater.*, **9**, 1803380 (2019).
42. Z. Choi, D. Kramer, and R. Mönig, *J. Power Sources*, **240**, 245 (2013).
43. T. Ohzuku, A. Ueda, and N. Yamamoto, *J. Electrochem. Soc.*, **142**, 1431 (1995).
44. M. Majima, S. Ujiie, E. Yagasaki, K. Koyama, and S. Inazawa, *J. Power Sources*, **101**, 53 (2001).
45. C. P. Sandhya, B. John, and C. Gouri, *Ionics*, **20**, 601 (2014).
46. B. Özdogru, H. Dykes, S. Padwal, S. Harimkar, and Ö. Ö. Çapraz, *Electrochim. Acta*, **353**, 136594 (2020).
47. H. Wang, X. Li, F. Li, X. Liu, S. Yang, and J. Ma, *Electrochem. Commun.*, **122**, 106870 (2021).
48. B. Tong, J. Wang, Z. Liu, L. Ma, Z. Zhou, and Z. Peng, *J. Power Sources*, **384**, 80 (2018).
49. T. R. Jow, S. A. Delp, J. L. Allen, J.-P. Jones, and M. C. Smart, *J. Electrochem. Soc.*, **165**, A361 (2018).
50. H. M. Dahn, A. J. Smith, J. C. Burns, D. A. Stevens, and J. R. Dahn, *J. Electrochem. Soc.*, **159**, A1405 (2012).
51. A. Raghavan et al., *J. Power Sources*, **341**, 466 (2017).
52. A. Ganguli et al., *J. Power Sources*, **341**, 474 (2017).
53. L. Albero Blanquer, F. Marchini, J. R. Seitz, N. Daher, F. Bétermier, J. Huang, C. Gervillié, and J.-M. Tarascon, *Nat. Commun.*, **13**, 1153 (2022).
54. S. Saxena, Y. Xing, D. Kwon, and M. Pecht, *Int. J. Electr. Power Energy Syst.*, **107**, 438 (2019).
55. P. Liu, J. Wang, J. Hicks-Garner, E. Sherman, S. Soukiazian, M. Verbrugge, H. Tataria, J. Musser, and P. Finamore, *J. Electrochem. Soc.*, **157**, A499 (2010).